NASA Technical Memorandum 84667

HEAT-TRANSFER DISTRIBUTIONS ON BICONICS AT INCIDENCE IN HYPERSONIC-HYPERVELOCITY He, N_2, AIR, AND CO_2 FLOWS

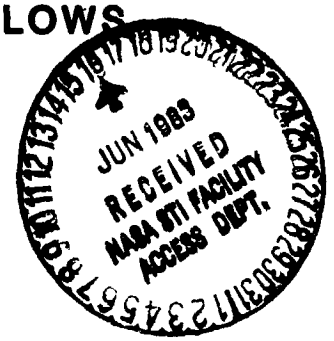

Charles G. Miller
John R. Micol
Peter A. Gnoffo
Sue E. Wilder

May 1983

National Aeronautics and Space Administration

Langley Research Center
Hampton, Virginia 23665

HEAT-TRANSFER DISTRIBUTIONS ON BICONICS AT INCIDENCE IN HYPERSONIC-HYPERVELOCITY He, N_2, AIR, AND CO_2 FLOWS

Charles G. Miller,* John R. Micol,**
Peter A. Gnoffo†, and Sue E. Wilder††
NASA Langley Research Center
Hampton, Virginia 23665

Abstract

Laminar heat-transfer rates were measured on spherically blunted, 13°/7° on-axis and bent biconics (fore cone bent 7° upward relative to aft cone) at hypersonic-hypervelocity flow conditions in the Langley Expansion Tube. Freestream velocities from 4.5 to 6.9 km/sec and Mach numbers from 6 to 9 were generated using helium, nitrogen, air, and carbon dioxide test gases, resulting in normal shock density ratios from 4 to 19. Angle of attack, referenced to the axis of the aft cone, was varied from zero to 20° in 4° increments. The effect of nose bend, angle of attack, and real-gas phenomena on heating distributions are presented along with comparisons of measurement to prediction from a code which solves the three-dimensional "parabolized Navier-Stokes" equations.

Nomenclature

C^*	defined as $\mu^* T_\infty / \mu_\infty T^*$
C_h	heat-transfer coefficient, $\dot{q}/(h_{t,2} - h_w)$, J-sec/m^4
h	enthalpy, J/kg
L	model length, m
M	Mach number
p	pressure, N/m^2
$\dot{q}$	heat-transfer rate, W/m^2
r	radius, m
R	unit Reynolds number, m^{-1}
St	Stanton number, $C_h/\rho_\infty U_\infty$
t	time, sec
T	temperature, K
T^*	reference temperature, $(T_{t,2}/6)(1+3T_w/T_{t,2})$, K, Ref. 41
U	velocity, m/sec
$\bar{v}^*$	viscous interaction parameter, $C^* M_\infty / \sqrt{Re_{\infty,L}}$
x,y,z	model coordinates (see Fig. 1), m
Z	moles of dissociated gas per moles of undissociated gas
α	angle of attack, deg
γ_E	isentropic exponent
μ	viscosity, N-sec/m^2
μ^*	viscosity evaluated at T^*, N-sec/m^2
ϕ	circumferential angle measured from the most leeward meridian, deg
ρ	density, kg/m^3
θ	cone half-angle, deg

Subscripts

a	aft-cone section
b	base
f	fore-cone section
m	measured
n	nose
s,10	incident shock into quiescent acceleration gas
sph	sphere
w	wall
2	static conditions immediately behind normal shock
t,2	stagnation conditions behind normal shock
∞	free-stream conditions

*Aero-Space Technologist, Aerothermodynamics Branch, Space Systems Division.
**Aerospace Engineer, Aerothermodynamics Branch, Space Systems Division.
†Aerospace Engineer, Aerothermodynamics Branch, Space Systems Division.
††Aero-Space Technologist, Aerothermodynamics Branch, Space Systems Division.

Introduction

Recent advances in navigation and knowledge of planetary atmospheres,[1-3] along with the need for Earth orbital transfer vehicles (OTV),[4-6] have rekindled interest in aerobraking and aerocapture techniques for proposed Earth and planetary missions. A generic vehicle proposed for missions to a number of planets[2,3] and a viable moderate lift-to-drag OTV candidate,[4-6] which also offers many advantages as a reentry

vehicle,[7] is a spherically-blunted biconic with the fore-cone section bent upward relative to the aft-cone section. Because of the scarcity of experimental data for bent biconics, a study was initiated at the Langley Research Center to establish a comprehensive data base. To date, aerodynamic coefficients, pressure distributions, oil-flow patterns, and shock shapes have been measured and reported on 2.9-percent scale models of the proposed configuration and this configuration without a bent nose (on-axis biconic).[8-10] These measurements have been made in three conventional-type, hypersonic wind tunnels, namely the 20-Inch Mach 6 Tunnel, Continuous Flow Hypersonic Tunnel, and Hypersonic CF_4 Tunnel, thereby providing a range of Mach number, Reynolds number, and normal shock density ratio (real-gas simulation parameter). Although a number of flowfield computer codes have been verified with this data base, heat-transfer measurements are required to determine if these codes accurately predict viscous effects.

The purpose of the present study is twofold: (1) to determine the effect of nose bend, angle of attack, and real-gas flow phenomena on heating distributions for the biconics; and (2) compare measurement with prediction. Because heat-transfer measurements for bent biconics are particularly scarce in the open literature, the present data represent a significant step toward achieving the goal of a complete and accurate data base for the validation of flowfield computer codes.

Experimental Method

Facility

The Langley Expansion Tube[11,12] is basically a 15.24-cm-diameter tube divided into three sections by two diaphragms; thus, this facility may be viewed as two shock tubes in tandem. Thick steel diaphragms separate the driver and intermediate sections, whereas a thin Mylar diaphragm separates the intermediate and acceleration sections. The isentropic, unsteady expansion resulting from the rupture of this thin Mylar diaphragm generates hypersonic and hypervelocity flow at the acceleration section exit from the low Mach number, shock-tube flow which encounters the secondary diaphragm. A detailed description of this facility is presented in Ref. 11, and calibration results are presented in Refs. 12 to 14.

Models

A planform view and dimensions of the biconic models are shown in Fig. 1, and a photograph of the bent biconic model installed in the test section of the expansion tube is shown in Fig. 2. The bent-biconic model represents a 1.9-percent scale of the proposed Mars sample return, single-mission vehicle.[2] The models were fabricated from stainless steel except for the nose tips, which were fabricated from MACOR, a machinable glass-ceramic.[15] Each model contained five slots for MACOR[15] substrates, the surfaces of which were contoured to the respective conic section. Two slots were machined along the most windward ray, two along the most leeward ray, (one on the fore cone and one on the aft cone), and one along the 90° ray on the aft cone.

Instrumentation

Heat Transfer. Thin-film resistance gages[16,17] were used to measure heat-transfer rates during the 250-microsecond test period of the expansion tube. Eight palladium gages, each approximately 1200 Å thick, were deposited along the polished surface of each MACOR substrate; a single thin-film gage was deposited at the spherical nose tip. Each gage was in the form of a serpentine pattern, as shown in Ref. 16, and provided nearly a point measurement since the sensing surface was 1.02 mm by 1.27 mm. Gages were covered with Al_2O_3 approximately 5000 Å thick to prevent the gage from becoming electrically shorted due to the ionized flow over the model. A constant current of 2 mA was maintained through each gage, which is sufficiently low to avoid ohmic heating effects.[16]

Heat-transfer rates on the nose, windward ray of the fore cone, and every other gage on the windward ray of the aft cone were determined by numerically integrating the surface temperature change as a function of time.[16,18] This method accounts for the variation of substrate thermal properties with temperature or time. Heat-transfer rates for the remaining gages were obtained using the analog circuit described in Ref. 17; the surface temperature for these gages was sufficiently low so to not require a significant correction to the heating rate because of changes in the thermal properties of the MACOR substrates.[16] Signals from the thin-film gage on the spherical nose and the 32 gages located along the most windward and leeward rays were recorded at 400 kHz (2.5 microseconds between data samples) with a transient waveform recording system. Digital data from this analog-to-digital system were retrieved by a HP 9845 computer and reduced to time histories of the heating rate (Fig. 3). Output signals for the eight thin-film gages located along the 90° ray were recorded from an oscilloscope with the aid of a camera.

Flow Visualization. Shock standoff distance was obtained using a single-pass schlieren system with a Xenon arc lamp as a light source. This point light source, having a duration of approximately 150 nanoseconds, was discharged just prior to termination of the useful test period.[12] (See Fig. 3.) Representative schlieren photographs are shown in Fig. 4.

Facility Flow Quantities. Incident shock velocity at the tube exit (test section) was determined by applying a least-squares curve fit to the average shock velocity between successive instrumented stations.[19] The time for the shock to travel between stations was obtained from counter-timer readings of the "stop" signals supplied by pressure transducers and heat-transfer gages mounted flush with the tube wall. Tube wall pressures and pitot pressures were measured using piezoelectric (quartz) transducers in conjunction with charge amplifiers. (It should be noted at this point that pitot pressures were measured during calibration tests performed prior to this study but were not measured for tests with the biconic models, as discussed subsequently.) Freestream static pressure was inferred from a transducer located 1.7-m upstream of the tube exit; the variation in

static pressure between this station and the tube exit is expected to be small (within experimental uncertainty).

Test Conditions

Facility. For the present tests, the driver gas was unheated hydrogen at a nominal pressure of 4.14 MN/m^2. The double diaphragm mode of operation was employed to reduce randomness in the pressure ratio across the primary diaphragm at time of rupture. Test gases were helium, nitrogen, dry air, and carbon dioxide. For a given test, the acceleration gas was the same as the test gas, but at a lower initial pressure.[12] Flow conditions for this study correspond to the optimum flow,[12] and no attempt was made to operate the facility at off-optimum conditions for any of the test gases in order to match Mach number and/or Reynolds number.

Flow conditions were determined using the thermochemical equilibrium program of Ref. 20, which has been modified to include helium. Inputs were freestream static pressure, freestream velocity, and pitot pressure. (Freestream static pressure was assumed equal to the measured tube wall pressure near the tube exit, freestream velocity was assumed equal to the incident shock velocity at the tube exit,[14,21] and pitot pressure corresponds to a mean value across the inviscid test core as inferred from tests with a pitot pressure survey rake performed prior to the present study.) Nominal values of measured inputs to the program of Ref. 20 and the corresponding freestream and post-normal shock flow conditions are given in Table 1. Based on the findings of Ref. 21, the freestream flow for helium, air, and CO_2 is assumed to be in thermochemical equilibrium; this assumption is also made for nitrogen test gas. Because of the relatively small values of freestream Reynolds number and small model size, laminar flow over the models is expected for all test gases.

Models. The models were tested at angles of attack from zero to 20°, where angle of attack is referenced to the axis of the aft-cone section. Both biconic models were tested for $0° \leq \alpha \leq 20°$ in 4° increments in air; for the other three test gases, the biconics were tested at α = 0°, 4°, 12°, and 20°. The on-axis biconic was rolled at α = 12° in air to provide a more detailed circumferential heating distribution. At α = 0° the spherical nose tip of the on-axis biconic was located 1.27 cm downstream of the tube exit. Based on unpublished calibration results, these relatively long models were located within the inviscid test core for all angles of attack and located in a region free of axial variation of flow properties.

Data Reduction and Uncertainty

Heat Transfer. The numerical method used to compute heat-transfer rates from the output of the thin-film resistance gages is discussed in Ref. 16, and the analog method is discussed in Ref. 17. Also included in Ref. 16 is a discussion of the calibration procedure used to determine the temperature coefficient of resistance of each gage and contributors to the uncertainty in the heat-transfer rate inferred from thin-film gages. Primary contributors for the present study are believed to be the uncertainty in the thermal properties of MACOR,[16] changes that occurred in gage properties for gages that were used in successive tests without recalibration, and the poor signal-to-noise ratio experienced during a number of tests.

Considering the probable sources of errors discussed in Ref. 16, the maximum uncertainty in measured heat-transfer rate for any given gage and test is believed to be less than 15 percent. The rms uncertainty in measured heat-transfer rate for both biconic models and all four test gases is 8 percent. Although an 8-percent uncertainty in heating along the most windward ray is believed realistic, a larger uncertainty is expected on the leeward ray, particularly at high angles of attack. This is due to the lower values of heating on the leeward ray and the nature of the flow in this complex, viscous-dominated flow region at high α.

Shock Shape. The shock detachment distance from the model surface was read manually from the schlieren photographs using a digitizing system having a sensitivity of 100 counts per 2.54 mm. The maximum uncertainty in measured shock detachment distance is believed to be less than 5 percent.

Flow Conditions. Uncertainties in the measured and calculated nominal freestream and post-shock flow conditions for the four test gases depend primarily on: (1) the precision associated with the measurement of the tube wall static pressure p_w, incident shock velocity $U_{s,10}$, and pitot pressure $p_{t,2}$, (2) run-to-run repeatability of these quantities, always a primary concern with impulse-type facilities, and (3) the validity of the assumptions made concerning the use of these measurements.

Careful and frequent calibrations of the pressure transducers demonstrated that measured values of p_w and $p_{t,2}$ are accurate to within 10 percent and 6 percent, respectively. Shock velocity $U_{s,10}$ is believed accurate to within 2.5 percent.[21] Nominal values of measured p_w and $U_{s,10}$ for each test gas were obtained from calibration tests with a pitot pressure survey rake, performed prior to this study, and from tests with the biconic models. Because the inviscid test core diameter is only 7.6 to 8.9 cm,[12,14] the relatively large models prohibited installation of a pitot pressure probe in the inviscid test core without disturbing the model flowfield. Thus, the nominal value of pitot pressure presented in Table 1 for each test gas was inferred from previous unpublished calibrations with a hydrogen driver. This procedure for determining flow conditions is the same as used in Ref. 21 for a helium driver.

Data scatter between the various calibration runs and runs with the biconic models was small (less than 8 percent for p_w and $p_{t,2}$ and 3.5 percent for $U_{s,10}$) due primarily to the double-diaphragm mode of operation.[12] Now, based on unpublished pressure distributions measured on a sharp leading-edge flat plate for the four test gases, the assumption that $p_\infty = p_w$ is believed valid. However, the assumptions that

$U_\infty = U_{s,10}$ and U_∞ are constant with run time are subject to question.[22] The sensitivity of calculated freestream and post-shock flow conditions, including stagnation-point heat-transfer rate to a sphere, to these uncertainties in measured inputs are presented in Ref. 21.

Calculated Stagnation-Point Heat Transfer to a Sphere. Heating distributions on the biconics are presented in terms of the freestream Stanton number St_∞ and as the ratio of surface heat-transfer rate to predicted stagnation-point heat-transfer rate to a sphere with radius equal to the biconic nose radius, $\dot{q}/\dot{q}_{sph}$. The wall enthalpy h_w required to compute St_∞ corresponds to a wall temperature equal to 300 K. Values of $\dot{q}_{sph}$ for the four test gases were obtained from the thermochemical equilibrium calculations of Ref. 23 and are presented in Table 1.

Prediction Method

Heating distributions were computed using computer code that solves the steady, three-dimensional "parabolized Navier-Stokes equations."[24,25] This code requires supersonic flow above the boundary layer in the downstream marching direction from the starting plane of data at or in front of the sphere-cone junction. A total of 50 points were taken between the shock and surface along an axis-normal coordinate and the number of points in the boundary layer was varied with angle of attack to account for the thinning of the boundary layer. The circumferential increment was 4.74°.

At the time the data reduction phase of the present study was initiated, the PNS code was applicable only for perfect air. This code has since been modified to include helium and real air in thermochemical equilibrium. Only a few cases for real air have been run at the time of this writing, and these results must be viewed as preliminary.

Results and Discussion

The limited space of this report prohibits presenting all the data obtained for the two biconic models in the four test gases; thus, the effects of nose bond, angle of attack, and test gas are illustrated with sample longitudinal heating distributions and with summary plots. Because these data provide the opportunity to validate various perfect-gas and real-gas flowfield computer codes and recognizing the difficulty associated with the extraction of data from such a report, tabulations of the present data are available upon request. Before presenting the data, a few general comments will be made.

A primary purpose of this study was to examine real-gas effects, resulting from the excitation of vibration, dissociation, and ionization energy modes, on heating to biconics in gases corresponding to various planetary atmospheres. CO_2 was selected as a test gas since it is the primary constituent of Mars and Venus atmospheres, nitrogen is the primary constituent of Titan's atmosphere, and air is, of course, Earth's atmosphere. To provide a lower limit to the range of normal-shock density ratio and a means for comparison with perfect-gas flowfield predictions, helium was used as a test gas. Even at the present velocity of 6.9 km/s, helium was not ionized. Thus, the biconic models were tested in ideal-gas and real-gas flow environments in the same facility with the same instrumentation, data acquisition system, and data reduction procedures.

In general, the flow was observed to establish (C_h become essentially constant with time) on the windward side of both biconic models within 120 μs for all test gases and $0° < \alpha < 20°$. Flow establishment on the leeward side required more time, especially at the higher angles of attack where the flow is quite complex and viscous dominated,[26-28] and the output of the leeward gages was characterized by larger fluctuations with time. However, even at the highest value of α, there was evidence that the "coarse" inviscid flow and finer viscous-flow structure about the model generally established, achieving a steady state within 200 μs. Thus, the heating distributions presented herein are assumed to represent a fully established flow condition.

To avoid or minimize the effects of surface temperature discontinuities on measured heat-transfer rates,[29] the thermal conductivities of the substrates and models should be matched as close as possible. Another concern at the high enthalpies of this study is the difference in surface catalycity between the MACOR substrates and the stainless-steel models.[30,31] Because of these concerns, the model was covered with a relatively thick deposit of Paralene C or sprayed with Krylon, a crystal-clear acrylic, prior to installation of the substrates. (It should be noted that windward substrates were generally destroyed during the post-run period and the cover badly sandblasted; thus, the models were removed from the facility after each run, recovered, and new substrates installed.) The effect of removing the cover is shown in Fig. 5 for the bent biconic in air. Removing the cover produced no significant effect on heating. One possible explanation for this good agreement is the thin-film gages were placed a sufficient distance from the material mismatches in the model surface to allow the flow to adjust, if necessary, to the MACOR surfaces. For the sake of continuity and the fact the cover provided excellent protection of the model surface from solid contaminants carried in the post-test flow, the model was covered for all runs.

Because of the relatively small model size and close proximity of the shock to the model surface at the higher density ratios, the flow within the shock layer may depart from equilibrium. This is especially true in the nose region. The results of Ref. 21, based on binary scaling for blunt bodies, revealed that the product of freestream density and predicted equilibrium shock standoff distance at the stagnation point must exceed 10^{-5} kg/m^2 to avoid significant nonequilibrium flow effects. For the biconic spherical nose radius of 3.83 mm, this product is less than 1.3×10^{-6} kg/m^2 for the three dissociated test gases, thus well within the nonequilibrium flow regime.

At sufficiently low Reynolds numbers, the shock and boundary-layer thicknesses are no longer negligible compared with the shock detachment distance.[21] A number of researchers have suggested various criteria in an effort to define the regimes between continuum and free molecular flow,[32] but these are only approximations. The parameter $\sqrt{Re_{2,rn}}/(\rho_2/\rho_\infty)^2$ (see Ref. 33) was selected to estimate the viscous effects for the flow over the spherical nose. According to this parameter, which varies from a low of 2.6 for CO_2 to a high of 23 for helium, the present flow over the nose is just within the slip flow regime.[3,33] In this regime, relatively small changes in Reynolds number may result in large changes in surface heating. The increase in heating over the continuum value is small (< 5 percent, or so) for helium, but may be significant for the other test gases, particularly CO_2. Although this parameter accounts for real-gas effects via use of ρ_2/ρ_∞,[21] it does not include the effect of wall temperature ratio $T_w/T_{t,2}$. The present large wall cooling tends to decrease the boundary-layer thickness, hence diminish rarefaction effects.[21]

Effect of Nose Bend

Bending the fore-cone section upward provides aerodynamic advantages[2,3] because of the asymmetry, but at an expected penalty in higher heating rates to the fore-cone section. To examine effects of this nose bend, heating distributions for the bent biconic are compared to the on-axis biconic in Figs. 6 and 7 for various angles of attack. Longitudinal heating distributions along the most windward and leeward rays are shown for air in Fig. 6. The ratio of windward heat-transfer coefficient for the bent biconic to that for the on-axis biconic is shown in Fig. 7 for all four test gases. These results (Fig. 7) were obtained from curve fits to the data to smooth the results and account for any missing thin-film gages for a particular run.

Noticeably lacking from the fore-cone heating distributions at $\alpha = 0°$ for all test gases was the overexpansion-recompression trend observed in the pressure distributions for these biconics at Mach 6 and Mach 10[8-10] and attributed to the surface discontinuity at the sphere-cone junction. For laminar flow, heating is expected to follow the trend in pressure;[34,35] however, the Mach 10 results of Refs. 36 and 37 imply that the present heating distributions should be free of such trends for $x/L > 0.25$. The decrease in windward heating due to the expansion at the junction scales roughly with the surface inclination change. That is, between the last gage on the fore cone and first gage on the aft cone, St_∞ decreases roughly 1.3 to 1.5 for the on-axis biconic (surface inclination change of 5.8°) and approximately twice this for the bent biconic (change of 12.8°, or twice that of the on-axis biconic) for all four test gases.

On the leeward side, bending the nose upward at $\alpha = 0°$ causes a larger variation in heating with z/L on the most leeward ray of the fore cone, smaller variation on the aft cone, and a decrease in heating by a factor of 2 to 3 for all test gases. When α is increased to 4°, corresponding to the leeward side of the bent biconic being nearly shielded from the flow, the heating distributions for the two biconics begin to converge with increasing distance from the nose tip. At $\alpha = 12°$ (Fig. 6(b)), corresponding to the on-axis biconic leeward side being almost shielded from the flow and the bent biconic being fully shielded, heating still decreases with increasing x/L for the on-axis biconic but increases with z/L for the bent biconic. These trends cause the heating distributions for the two biconics to cross at about 40 percent of the body length. At $\alpha = 20°$ (Fig. 6(a)), leeward heating for the bent biconic exceeds that for the on-axis biconic in air. Similar trends were observed for the other gases and are consistent with leeward flow separation,[8-10,26-28,37] as will be discussed in the next section.

The penalty paid in increased windward fore-cone heating due to the nose bend is about 1.7 to 2 at $\alpha = 0°$ for the four test gases (Fig. 7(a)). However, the nose bend causes a decrease in windward aft-cone heating for air, N_2, and CO_2, whereas the heating for helium is essentially unaffected by the bend. This lower heating on the bent biconic aft cone for the dissociated test gases is believed due to: (1) the lower values of gamma within the shock layer for these gases, which result in a larger expansion at the junction, hence a lower aft-cone surface pressure,[10] and (2) nonequilibrium flow effects. At $\alpha = 12°$, the penalty in fore-cone heating due to the bend decreases to about 1.2 to 1.4 and to about 1.1 to 1.2 at $\alpha = 20°$. Heating on the aft cone is less for the bent biconic, including helium test gas, for $\alpha = 12°$ and 20°. Thus, although a penalty in windward heating to the fore cone occurs due to the nose bend, as expected, this penalty diminishes markedly with increasing α and is only 10 to 20 percent at the design trim angle of attack of 20° for the bent biconic.

Effect of Angle of Attack

Heating to the windward ray increases with angle of attack for both biconics and all test gases, as expected, but the relative effect of α on heating decreases with increasing α (Figs. 8 to 10). For the present range of α, the penalty in windward heating for the bent biconic is roughly a factor of 2 on the fore cone and a factor of 3 to 4 on the aft cone, being largest for helium test gas.

The effect of α on leeward heating is not nearly as orderly as on the windward side. Leeward heating for the on-axis biconic decreases as α is increased from 0° to 8°, but increases for $\alpha > 8°$. This trend was observed for all test gases and is attributed to flow separation and the formation of vortices.[8-10,26-28,37] The oil-flow patterns of Refs. 9 and 10 show that a "stagnation-line" type of flow is created on the most leeward ray by the mutual action of counter-rotating longitudinal vortices that reattach on this ray. For the low Reynolds numbers of this study, the leeward separated flow should be free of any secondary vortices.[10] This vortex reattachment results in the heating on the most leeward ray being higher than just off this ray, as evident from the circumferential heating distribution shown in Fig. 11 for the on-axis biconic at $\alpha = 12°$.

Effect of Test Gas

Shock shapes for the four test gases are compared in Fig. 12 for the bent biconic at α = 4°. The fact that the shock detachment distance for blunt bodies in hypersonic flows correlates in terms of a single parameter ρ_2/ρ_∞ is well known,[2,3,21] with the detachment distance decreasing with increasing density ratio. This decrease in shock detachment distance with increasing ρ_2/ρ_∞ also occurs for the relatively slender biconic models as shown in Fig. 12. The effect of density ratio on detachment distance was observed to diminish with increasing angle of attack on the windward and leeward sides; that is a lesser effect of ρ_2/ρ_∞ on windward shock-detachment distance occurs as the effective body becomes blunter. The trend on the leeward side is due to the shock inclination downstream of the nose region becoming more dependent on Mach number at the higher α.[8] The observed differences in shock detachment distance and inclination for the present test gases are expected to influence the variable edge-entropy effect caused by the mass "swallowed" or entrained by the boundary layer,[38,39] hence influence the heating distributions.

In examining the effects of nose bend and angle of attack on heating distributions, differences in Mach number, Reynolds number, density ratio or gamma, and wall temperature ratio were not considered explicitly. However, these quantities must be considered in any attempt to deduce the effect of test gas on heating. This adds complexity to the present study since the Expansion Tube was operated to yield the highest quality flow for each test gas and M_∞ and R_∞ were not matched for the four gases. For example, although the freestream Reynolds numbers for helium, air and CO_2 are relatively close, R_∞ for nitrogen is only half as large. Now, laminar heating on a reentry glider model has been correlated in terms of $St_\infty\sqrt{R_{\infty,L}}$ for high enthalpy flows.[40] Taking this a step further to account for differences in R_∞, M_∞, and $T_w/T_{t,2}$, the decision was made to present the present heating data in terms of $St_\infty/\bar{V}^*$. The viscous interaction parameter $\bar{V}^*$ is defined[32] as $C^*M_\infty/\sqrt{R_{\infty,L}}$, where $C^* \equiv \mu^*T_\infty/\mu_\infty T^*$ and T^* is a reference temperature,[41] $T^* = (T_{t,2}/6)(1+3T_w/T_{t,2})$. Heating distributions are also presented as the percent of stagnation-point heat-transfer rate to a sphere[23] having a radius equal to that of the spherical nose tip, $\dot{q}/\dot{q}_{sph}$. (Values of $\dot{q}_{sph}$ are presented in Table 1.) (Although $\dot{q}_{sph}$ is relatively insensitive to Mach number and Reynolds number, the ratio $\dot{q}/\dot{q}_{sph}$ may not be, and thus does not provide a means for separating M_∞, R_∞ effects from real-gas effects.)

Values of the heating ratio $\dot{q}/\dot{q}_{sph}$ for the four test gases are compared in Fig. 13 for the on-axis biconic. At zero incidence (Fig. 13(a)), $\dot{q}/\dot{q}_{sph}$ on the fore cone is nearly the same for air, N_2, and CO_2, all being higher than helium. As the flow expands at the fore-cone/aft-cone junction, the decrease in heating that occurs for CO_2 is greater than for the other three gases and $\dot{q}/\dot{q}_{sph}$ for CO_2 approaches that for helium. As discussed previously, this trend is attributed to gamma effects and possible nonequilibrium flow effects. The same trends in windward $\dot{q}/\dot{q}_{sph}$ are observed at α = 12° and 20°; however, the difference in $\dot{q}/\dot{q}_{sph}$ between the test gases decreases with increasing α, especially on the fore cone. At α = 12°, leeward $\dot{q}/\dot{q}_{sph}$ exhibits the same trend as observed on the windward side, but at α = 20°, this heating ratio for CO_2 is less than for the other gases. As a rule of thumb for the on-axis biconic, $\dot{q}/\dot{q}_{sph}$ on the windward aft cone is roughly half that on the windward fore cone and leeward values are an order of magnitude less than windward values.

Basically, the same trends in $\dot{q}/\dot{q}_{sph}$ were observed for the bent biconic as observed for the on-axis biconic. One notable exception was that $\dot{q}/\dot{q}_{sph}$ for CO_2 is lower than the other gases on the windward and leeward sides of the aft cone for all angles of attack. As with the on-axis biconic, $\dot{q}/\dot{q}_{sph}$ on the leeward side of the bent biconic for air and N_2 either agrees with or exceeds values for helium. One last point--windward aft-cone heating distributions in CO_2 at the higher angles of attack decrease monotonically downstream of the junction, but then increase in the direction of the base. Schlieren photographs in CO_2 (Fig. 4) revealed the shock over the aft cone on the windward side curved back toward the model surface in the region of the base. This minima in heating on the windward side of the aft cone is believed to be characteristic of low gamma flows since it was observed[10] in pressure distributions measured at Mach 6 in CF_4 (γ_{eff} = 1.13), but not at Mach 6 in air (γ = 1.4). It was also predicted for CF_4 using a perfect-gas, inviscid flowfield code with effective gamma as the input,[10] and predicted in Ref. 3 for CO_2.

In Figs. 14 and 15, windward $St_\infty/\bar{V}^*$ for air, nitrogen, and CO_2 is nondimensionalized by this ratio for helium. In this form, the results for CO_2 are consistently lower than for air or nitrogen for both biconics and $0° \leq \alpha \leq 20°$. The air and nitrogen results are generally in fair to good agreement for both biconics, particularly on the fore cone. This good agreement between air and nitrogen is expected, provided Reynolds number effects are properly accounted for, because of the similarity in gamma within the shock layer for these two gases, in Mach number, and in $T_w/T_{t,2}$. When these two gases are not in agreement on the aft cone, the air data usually exceed the nitrogen data, thereby implying a larger departure from equilibrium for nitrogen in the expansion at the junction. The ratio $St_\infty/\bar{V}^*$ for air, nitrogen and CO_2 is less than that for helium.

Due to the complexity of the present flow, it is difficult to separate Mach number, Reynolds number, gamma, and chemistry effects. Additional tests with these, or similar, models at various Mach numbers and Reynolds numbers in conventional, ideal-air wind tunnels are required to separate out the real-gas effects and determine if $\bar{V}^*$ accurately accounts for M_∞ and $R_{\infty,L}$ effects.

Comparison to Prediction

Comparisons of measured and predicted heating distributions in helium are shown in Figs. 16 and 17 for the on-axis biconic and bent

biconic, respectively. This code ran successfully for $0° < \alpha < 20°$ for the on axis biconic, but difficulties were encountered at the highest angle of attack for the bent biconic. The failure to run successfully at $\alpha = 20°$, corresponding to $\alpha_f = 27°$, is attributed to the proximity of the sonic line across the shock layer to the starting data plane on the windward side.[10] The stagnation-point heat-transfer rate measured at the spherical nose tip of the on-axis biconic in helium at $\alpha = 0°$ was predicted to within 3 percent by the starting solution[42] used for the PNS code. Heating rates on the on-axis biconic (Fig. 16) at $\alpha = 0°$ and 4° are accurately predicted by the PNS code. At $\alpha = 12°$, corresponding to a thinner boundary layer on the windward side (requires more points to accurately model the temperature distribution through the boundary layer) and separated, viscous-dominated flow on the leeward side, the PNS code slightly underpredicts windward and leeward heating. With the exception of a few points, the agreement is within 10 percent or within the experimental uncertainty. At $\alpha = 20°$, the underprediction of windward heating worsens and measurement and prediction diverge on the leeward side of the aft cone.

Turning to the bent biconic (Fig. 17), the PNS code again accurately predicts the heating distributions at $\alpha = 0°$ and 4° in helium. Windward aft-cone heating is accurately predicted for $0° \leq \alpha \leq 12°$, whereas windward fore-cone heating is underpredicted somewhat. At $\alpha = 12°$, the PNS code overpredicts leeward heating by as much as 15 to 20 percent. Thus, in general, when the leeward side is not fully shielded from the flow ($\alpha_f/\theta_f < 1$), the PNS code predicts windward and leeward heating with good accuracy. When the leeward side is shielded, resulting in vortex shedding, the PNS code tends to overpredict leeward heating.

Nonequilibrium flow effects were expected for these models in air, but it was hoped that comparisons to the PNS code with equilibrium real-air capability would furnish information on the degree to which nonequilibrium influenced the heating. The reasoning, somewhat oversimplified, was if the code was verified for helium flow and care taken to incorporate the real-air properties, then the code should provide the basis for deducing nonequilibrium flow effects. At the time of this writing only two air cases had been run for the on-axis biconic and both cases must be viewed as preliminary. At $\alpha = 0°$ and 4° (Fig. 18), measured and predicted heating on the fore cone tend to diverge with distance from the nose tip. Since the PNS code tended to underpredict heating in helium, this trend may be the result of a nonequilibrium expansion from the spherical nose onto the fore cone and the flow tending to equilibrate as it approaches the junction. Windward aft-cone heating is underpredicted by up to 25 percent for both angles of attack. Leeward heating on the fore cone is predicted quite well (within 10 percent) at $\alpha = 4°$, but the aft-cone heating is underpredicted 15 to 20 percent. The cause(s) for these underpredictions in air are not fully understood at this time and additional analysis is planned.

Concluding Remarks

Laminar heating distributions have been measured on spherically-blunted, 13°/7° on-axis and bent biconics in the Langley Expansion Tube. These data are unique since a given model was tested in several test gases at hypersonic and hypervelocity flow conditions. Test gases were helium, nitrogen, air, and carbon dioxide; free-stream Mach numbers ranged from 6 to 9 and velocities from 4.5 to 7 km/s. Even at these high velocities, helium behaved as an ideal gas, providing heating distributions that may be compared to ideal-gas theory. Preliminary analysis of these data revealed the following: (1) Although a penalty in windward heating to the fore cone due to the nose bend was observed, as expected, this penalty diminishes rapidly with increasing angle of attack and is only 10 to 20 percent at the design trim angle of attack of 20°. (2) Aft-cone windward heating was more sensitive to angle of attack than fore-cone heating, increasing by 3 to 4 as the angle of attack was increased from zero to 20° compared to 2 on the fore cone. (3) Leeward heating distributions initially decreased with increasing angle of attack, but then increased. This trend is attributed to flow separation on the leeward side and the formation of vortices when the fore-cone angle of attack exceeds the fore-cone half angle. (4) Heating on the windward side of the on-axis aft cone was roughly half that on the fore cone and the leeward heating was an order of magnitude less than the windward. (5) Several trends were attributed to real-gas phenomena, such as the decrease in aft-cone heating for CO_2 because of a nonequilibrium expansion at the fore-cone/aft-cone junction. However, Mach number, Reynolds number, wall temperature ratio, and gamma or density ratio varied for the four test gases. This makes it difficult to separate real-gas effects from effects that result from the variations and additional analysis is required in this area. Finally, (6) the PNS code predicts windward and leeward heating in helium to good accuracy when the leeward side is not shielded from the flow. When shielded, corresponding to vortex shedding on the leeward side, the PNS code tends to overpredict leeward heating. Preliminary results from the real-gas PNS code yielded somewhat poorer comparisons to data for air than those obtained by the perfect gas code for helium.

References

[1]Walberg, G. D., "A Review of Aeroassisted Orbit Transfer," AIAA Paper 82-1378, August 1982.

[2]Florence, D. E., "Aerothermodynamic Design Feasibility of a Mars Aerocapture/Aeromaneuver Vehicle," AIAA Paper 81-1127, June 1981.

[3]Florence, D. E., "Aerothermodynamic Design Feasibility of a Generic Planetary Aerocapture/Aeromaneuver Vehicle," AIAA Paper 81-1127, June 1981.

[4]Austin, R. E., Cruz, M. I., and French, J. R., "System Design Concepts and Requirements for Aeroassisted Orbital Transfer Vehicles," AIAA Paper 82-1379, August 1982.

[5]Letts, W. R., and Pelekanos, A., "Aeroassisted Orbital Transfer Mission Evaluation," AIAA Paper 82-1380, August 1982.

[6]Jamison, C. C., and Visentine, J. T., "Utilization of Shuttle Launched Research Vehicles for the Technical Validation of Advanced Earth and Planetary Atmospheric Entry Systems," AIAA Paper 82-1383, August 1982.

[7]Lin, T. C., and Grabowsky, W. R., "The Search of Optimum Configurations for Reentry Vehicles," AIAA Paper 82-1303, August 1982.

[8]Miller, C. G., and Gnoffo, P. A., "Pressure Distributions and Shock Shapes for 12.84°/7° On-Axis and Bent-Nose Biconics in Air at Mach 6," NASA TM 83222, December 1981.

[9]Miller, C. G., and Gnoffo, P. A., "An Experimental Investigation of Hypersonic Flow Over Biconics at Incidence and Comparison to Prediction," AIAA Paper 82-1382, August 1982.

[10]Miller, C. G., Blackstock, T. A., Helms, V. T., and Midden, R. E., "An Experimental Investigation of Control Surface Effectiveness and Real-Gas Simulation for Biconics," AIAA Paper 83-0213, January 1983.

[11]Moore, J. A., "Description and Initial Operating Performance of the Langley 6-Inch Expansion Tube Using Heated Helium Driver Gas," NASA TM X-3240, September 1975.

[12]Miller, C. G., "Operational Experience in the Langley Expansion Tube With Various Test Gases," NASA TM 78637, December 1977.

[13]Miller, C. G., "Flow Properties in Expansion Tube with Helium, Argon, Air, and CO_2," AIAA Journal, Vol. 12, No. 4, April 1974, pp. 564-566.

[14]Shinn, J. L., and Miller, C. G., "Experimental Perfect-Gas Study of Expansion-Tube Flow Characteristics," NASA TP 1317, December 1978.

[15]Grossman, D. G., "Machining a Machinable Glass-Ceramic," Vacuum, Vol. 28, No. 2, February 1978, pp. 55-61.

[16]Miller, C. G., "Comparison of Thin-Film Resistance Heat-Transfer Gages With Thin-Skin Transient Calorimeter Gages in Conventional Hypersonic Wind Tunnels," NASA TM 83197, December 1981.

[17]Reddy, N. M., "Heating-Rate Measurements Over 30° and 40° (Half-Angle) Blunt Cones in Air and Helium in the Langley Expansion Tube Facility," NASA TM 80207, March 1980.

[18]Cook, W. J., "Determination of Heat-Transfer Rates From Transient Surface Temperature Measurements." AIAA Journal, Vol. 8, No. 7, July 1970, pp. 1366-1368.

[19]Miller, C. G., and Jones, J. J., "Incident Shock-Wave Characteristics in Air, Argon, Carbon Dioxide, and Helium in a Shock Tube With Unheated Helium Driver," NASA TN D-809, December 1975.

[20]Miller, C. G., "Computer Program of Data Reduction Procedures for Facilities Using CO_2-N_2-O_2-Ar Equilibrium Real-Gas Mixtures," NASA TM X-2512, March 1972.

[21]Miller, C. G., "Shock Shapes on Blunt Bodies in Hypersonic-Hypervelocity Helium, Air, and CO_2 Flows, and Calibration Results in Langley 6-Inch Expansion Tube," NASA TN D-7800, February 1975.

[22]Friesen, W. J., "Use of Photoionization in Measuring Velocity Profile of Free-Stream Flow in Langley Pilot Model Expansion Tube," NASA TN D-4936, December 1968.

[23]Sutton, K., and Graves, R. A., "A General Stagnation-Point Convective-Heating Equation for Arbitrary Gas Mixtures," NASA TR R-376, November 1972.

[24]Vigneron, Y. C., Rakich, J. V., and Tannehill, J. C., "Calculation of Supersonic Viscous Flow Over Delta Wings With Sharp Subsonic Leading Edges," AIAA Paper 78-1137, July 1978.

[25]Agarwal, R., and Rakich, J. V., "Supersonic Laminar Viscous Flow Past a Cone at Angle of Attack in Spinning and Coning Motion," AIAA Journal, Vol. 20, No. 6, June 1982, pp. 761-768.

[26]Stetson, K. R., "Boundary-Layer Separation on Slender Cones at Angle of Attack," AIAA Journal, Vol. 10, No. 5, May 1972, pp. 642-648.

[27]Rainbird, W. J., "Turbulent Boundary-Layer Growth and Separation on a Yawed Cone," AIAA Journal, Vol. 6, No. 12, December 1968, pp. 2410-2416.

[28]Rainbird, W. J., Crabbe, R. S., Peake, D. J., and Meyer, R. F., "Some Examples of Separation in Three-Dimensional Flow," Canadian Aeronautics and Space Journal, December 1966, pp. 409-423.

[29]Schultz, D. L., and Jones, T. V., "Heat-Transfer Measurements in Short-Duration Hypersonic Facilities," AGARD-AG-165, February 1973.

[30]Anderson, L. A., "Effect of Surface Catalytic Activity on Stagnation Heat-Transfer Rates," AIAA Journal, Vol. 11, No. 5, May 1973, pp. 649-656.

[31]Shinn, J. L., Moss, J. N., and Simmonds, A. L., "Viscous-Shock-Layer Heating Analysis for the Shuttle Windward Symmetry Plane with Surface Finite Catalytic Recombination Rates," AIAA Paper 82-0842, June 1982.

[32]Little, H. R., "An Experimental Investigation of Surface Conditions on Hyperboloids and Paraboloids at a Mach Number of 10," AEDC-TR-69-225, January 1970.

[33]Gilbert, L. M., and Goldberg, L., "A Reynolds Number Scaling Theory for Hypersonic Ablation," AIAA Paper 67-155, January 1967.

[34]Widhopf, G. F., "Heat-Transfer Correlations for Blunt Cones at Angle of Attack," Journal of Spacecraft and Rockets, Vol. 8, No. 9, September 1971, pp. 1002-1004.

[35]Griffith, B. J., and Lewis, C. H., "Laminar Heat Transfer to Spherically Blunted Cones at Hypersonic Conditions," AIAA Journal, Vol. 2, No. 3, March 1964, pp. 438-444.

[36]Cleary, J. W., "Effects of Angle of Attack and Bluntness on Laminar Heating-Rate Distributions of a 15° Cone at a Mach Number of 10.6," NASA TN D-5450, October 1969.

[37]Dearing, D. J., "Laminar Heat-Transfer Distributions for a Blunted-Cone, Cone-Frustum Reentry Configuration at Mach 10," NASA TN D-5146, April 1969.

[38]Adams, J. C., Martindale, W. R., Mayne, A. W., and Marchand, E. O., "Real-Gas Scale Effects on Hypersonic Laminar Boundary-Layer Parameters Including Effects of Entropy-Layer Swallowing," AEDC-TR-75-2, December 1975.

[39]Griffith, B. J., and Majors, B. M., "Hypersonic Turbulent Boundary-Layer Parameters on Spherically Blunted Cones, Including Entropy Layer Swallowing and Real-Gas Effects," AIAA Paper 81-1089, June 1981.

[40]Stalker, R. J., "Development of a Hypervelocity Wind Tunnel," Aeronautical Journal of the Royal Aeronautical Society, June 1972, pp. 374-384.

[41]Cheng, H. K., "Hypersonic Flow With Combined Leading-Edge Bluntness and Boundary-Layer Displacement Effect," CAL Report No. AF-1285-A-4, August 1960.

[42]Gnoffo, P. A., "A Vectorized, Finite-Volume, Adaptive Grid Algorithm Applied to Planetary Entry Problems," AIAA Paper No. 82-1018, June 1982.

Table 1. Nominal Flow Conditions

Free-stream

Test Gas	p_∞, N/m^2	ρ_∞, kg/m^3	T_∞, K	$\gamma_{E,\infty}$	U_∞, m/sec	M_∞	R_∞, m^{-1}
Helium	1300	1.72×10^{-3}	364	1.667	6900	6.15	4.87×10^{5}
Nitrogen	1635	2.88	1913	1.302	5515	6.41	2.62
Air	2182	4.73	1604	1.296	5326	6.89	4.50
CO_2	1030	5.09	1070	1.179	4535	9.29	5.64

Post-Normal Shock

Test Gas	$p_{t,2}$, kN/m^2	$\rho_{t,2}$, kg/m^3	$T_{t,2}$, K	$\gamma_{E,t,2}$	$Z_{t,2}$	$h_{t,2}$, MJ/kg	h_w, MJ/kg	$\frac{\rho_2}{\rho_\infty}$	$\dot{q}_{sph, Ref. 23}$, MW/m^2
Helium	72.6	0.71×10^{-2}	4948	1.667	1.00	25.69	1.56	3.71	26.28
Nitrogen	85.6	3.55	6471	1.127	1.26	17.41	.31	11.83	28.22
Air	130.35	5.49	6162	1.143	1.34	15.96	.30	11.13	31.92
CO_2	103.0	9.83	3531	1.132	1.57	2.41	-8.72	18.83	21.92

Note: h_w evaluated at T_w = 300 K.
Z_∞ = 1 for all test gases.

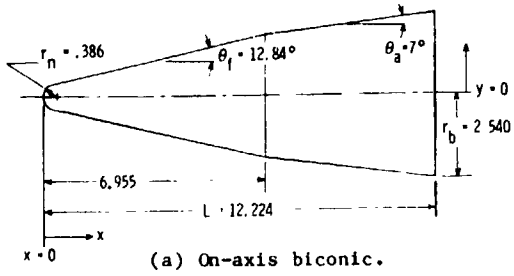

(a) On-axis biconic.

Fig. 1 Planform view and dimensions of models. All dimensions in cm.

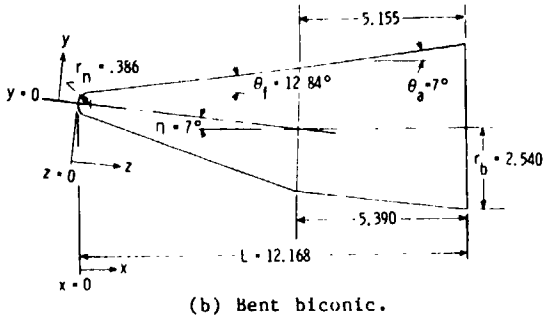

(b) Bent biconic.

Fig. 1 Concluded.

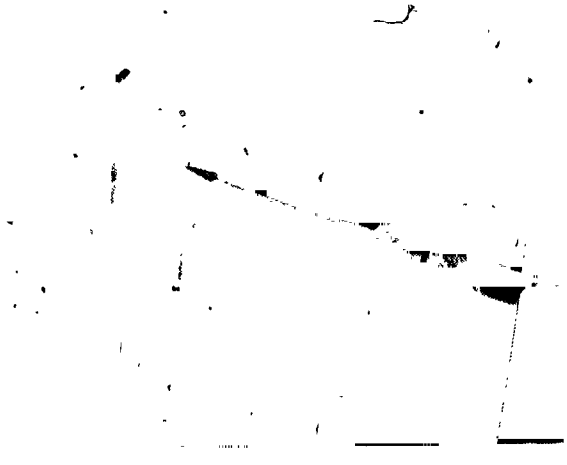

Fig. 2 Photograph of bent biconic model.

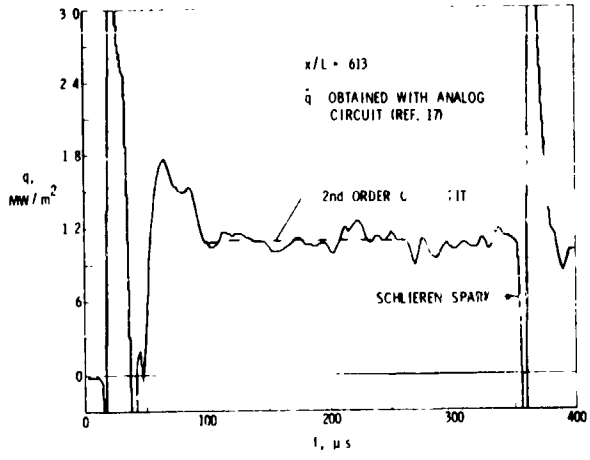

Fig. 3 Time history of heat-transfer rate on leeward ray of on-axis biconic in air at α = 4°.

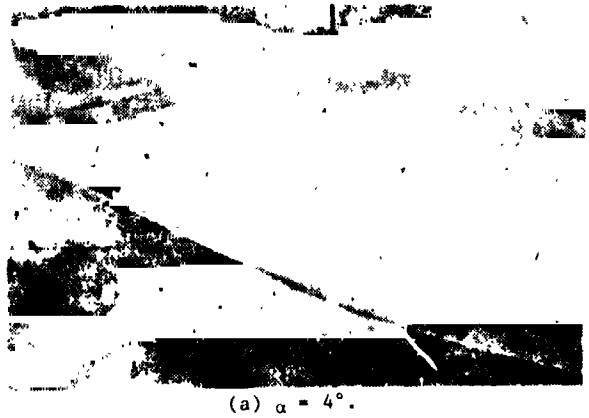

(a) α = 4°.

Fig. 4 Representative schlieren photographs for bent biconic in CO_2.

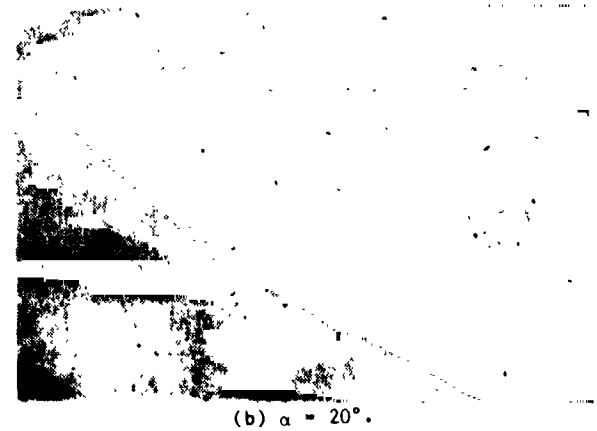

(b) α = 20°.

Fig. 4 Concluded.

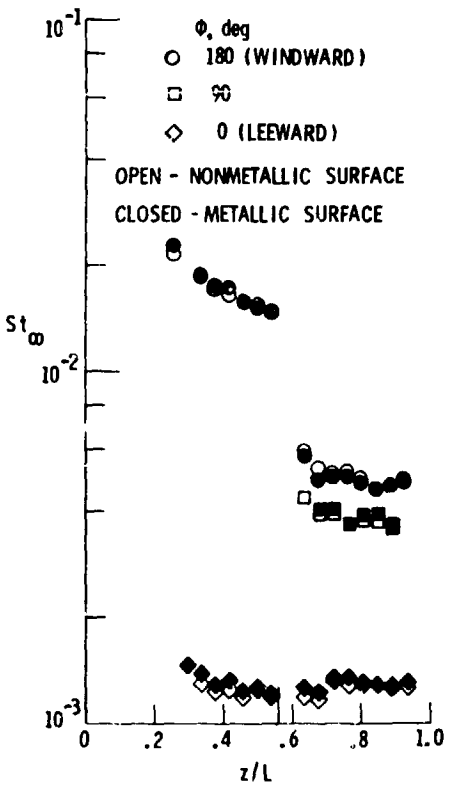

Fig. 5 Effect of model cover on heating for bent biconic in air at $\alpha = 8°$.

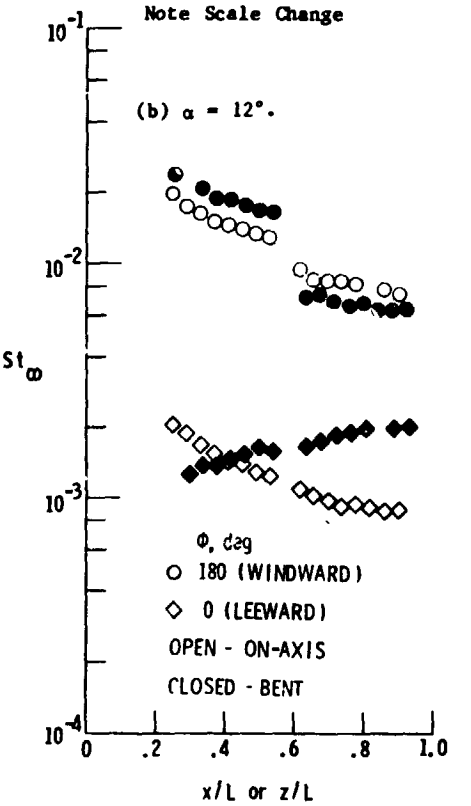

Fig. 6 Continued.

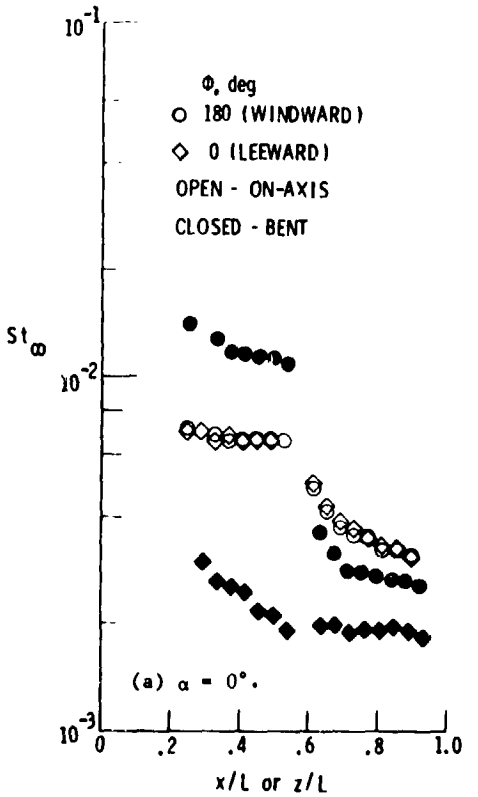

Fig. 6 Effect of nose bend on heating in air.

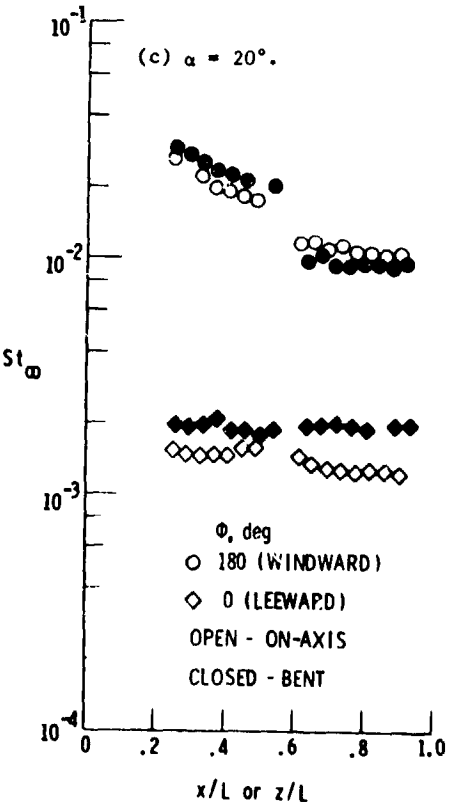

Fig. 6 Concluded.

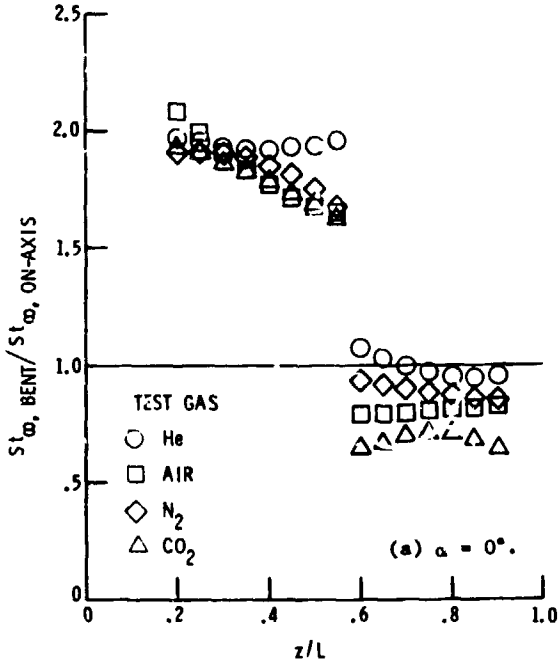

Fig. 7 Ratio of bent biconic to on-axis biconic heating for present test gases.

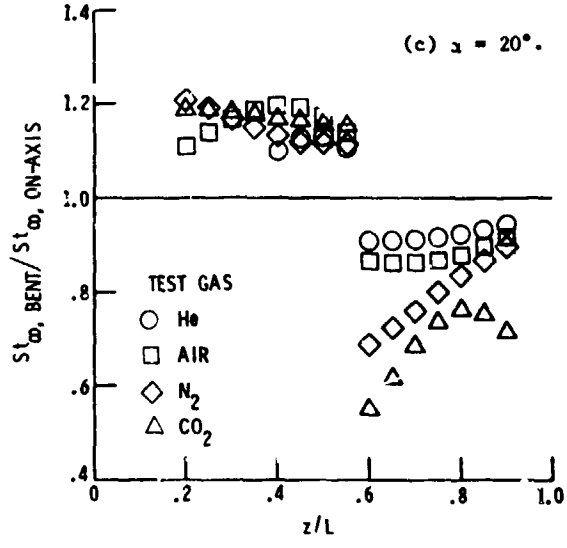

Fig. 7 Concluded.

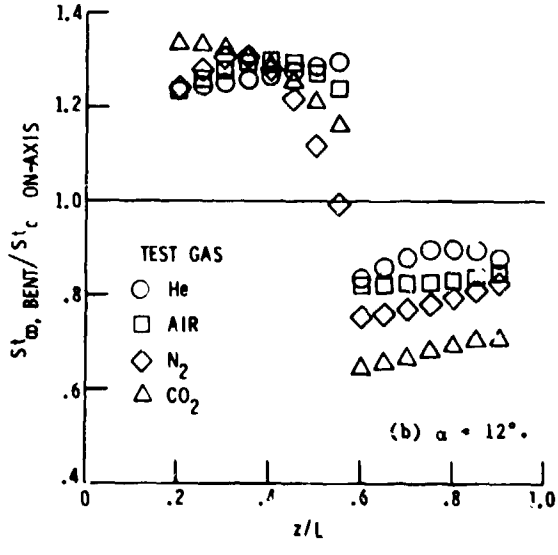

Fig. 7 Continued.

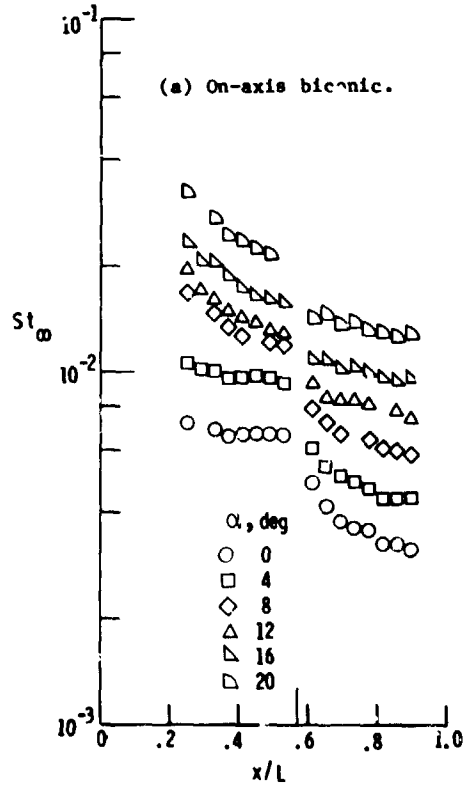

Fig. 8 Effect of angle of attack on windward heating in air.

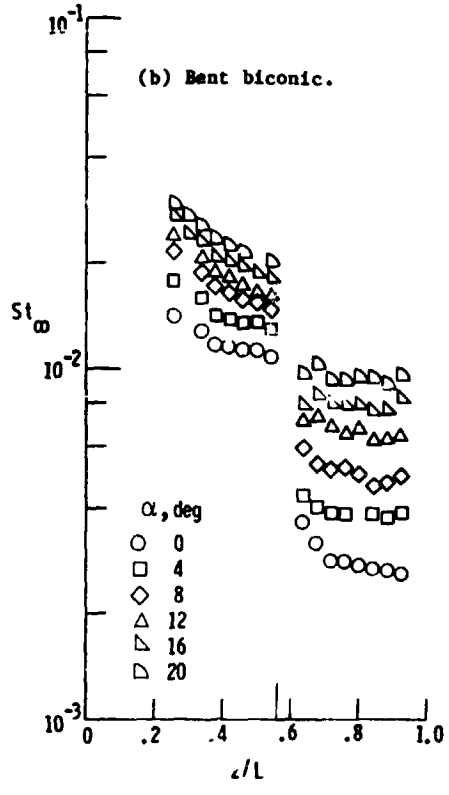

Fig. 8 Concluded.

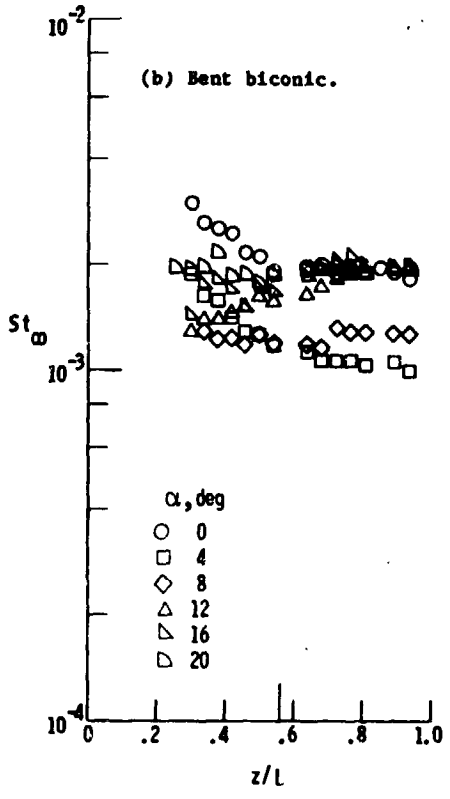

Fig. 9 Concluded.

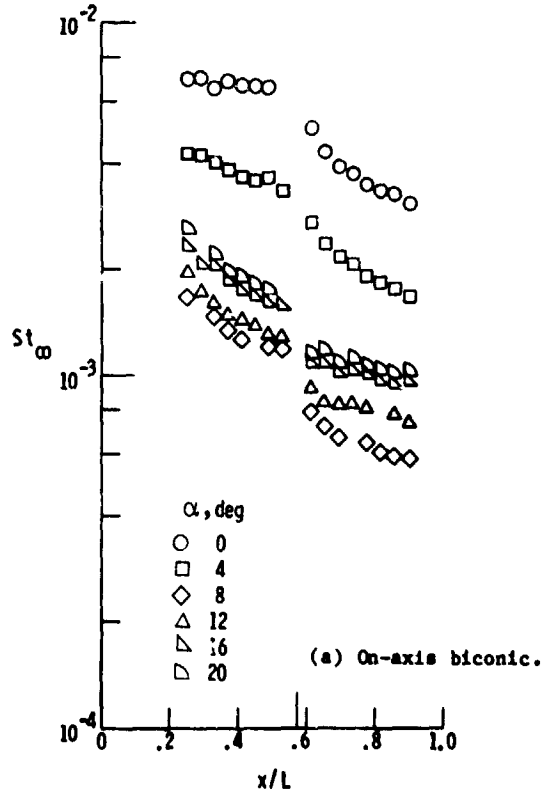

Fig. 9 Effect of angle of attack on leeward heating in air.

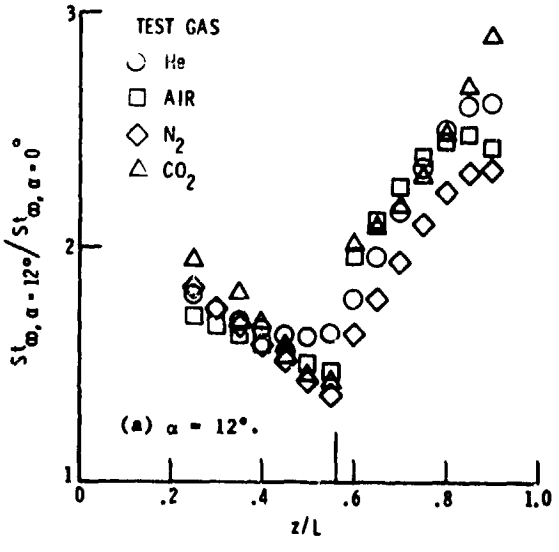

Fig. 10 Effect of angle of attack on windward heating to bent biconic for present test gases.

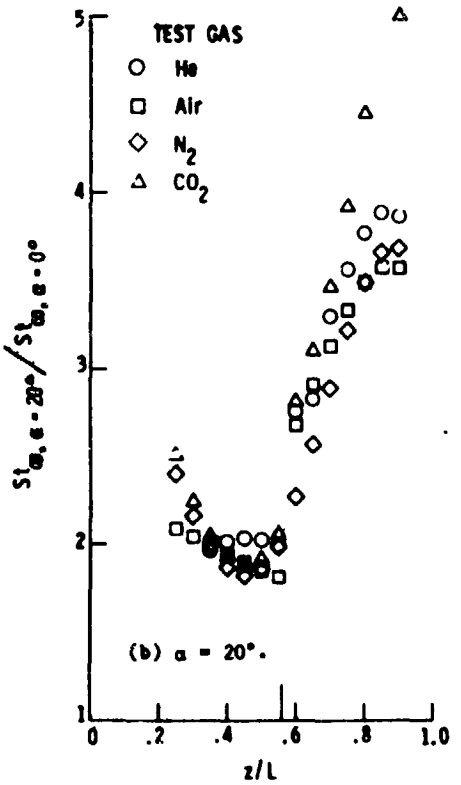

Fig. 10 Concluded.

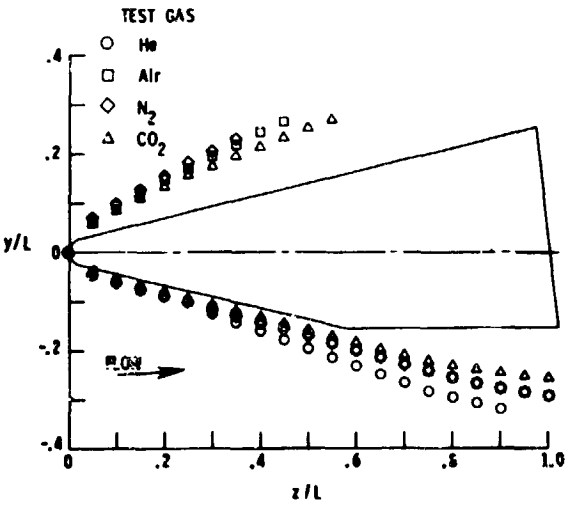

Fig. 12 Shock shapes for bent biconic at α = 4° in present test gases.

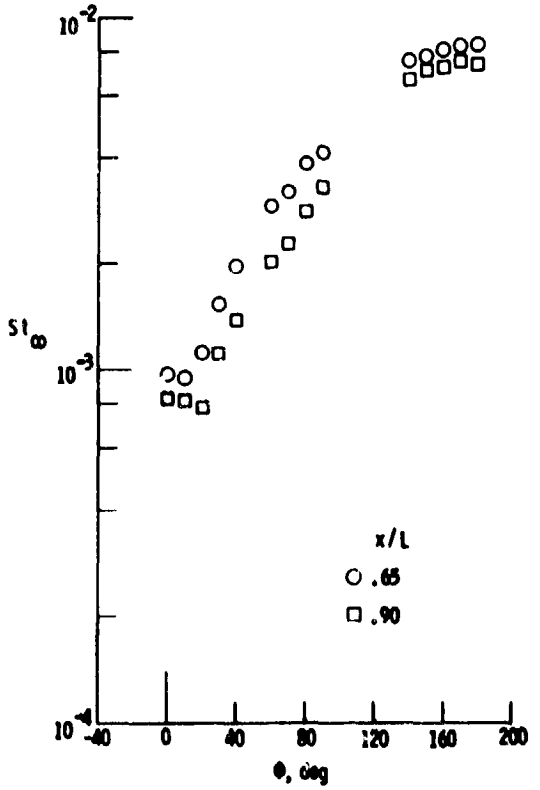

Fig. 11 Circumferential heating distribution for on-axis biconic in air at α = 12°.

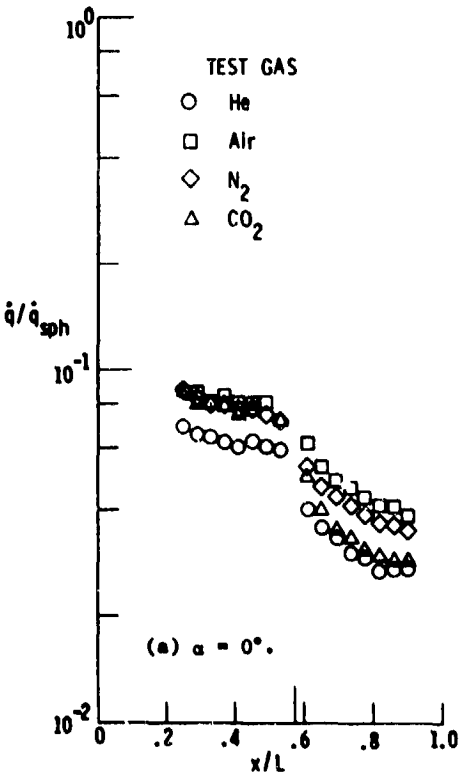

Fig. 13 Heating distributions for on-axis biconic in present test gases.

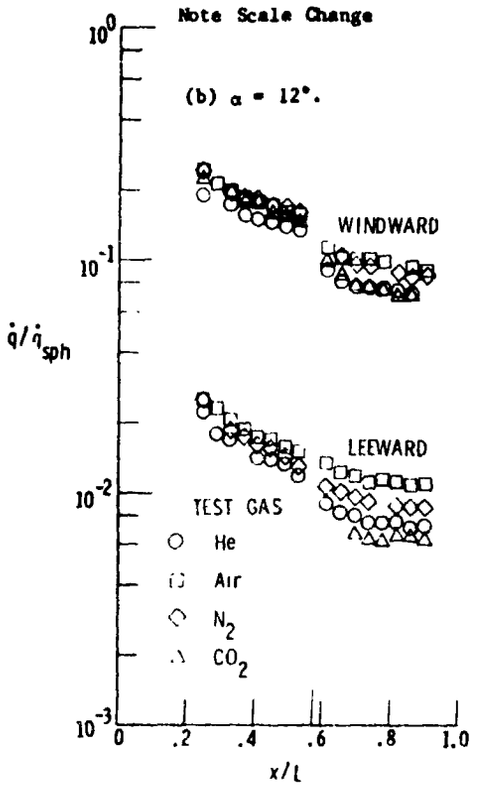

Fig. 13 Continued.

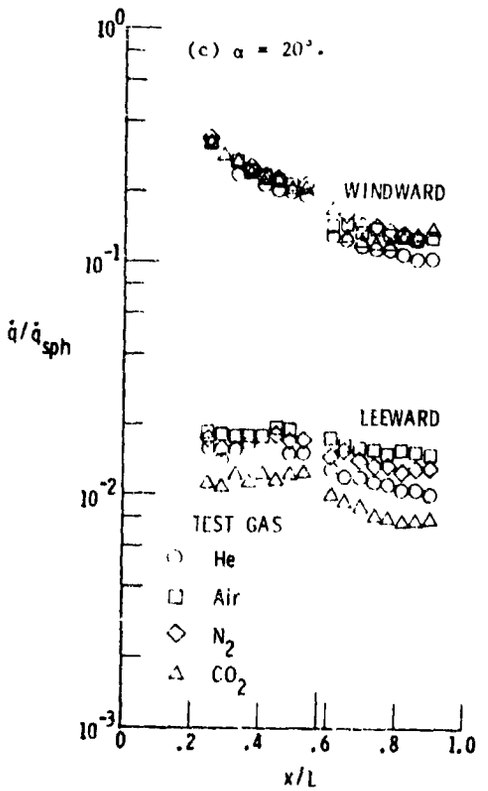

Fig. 13 Concluded.

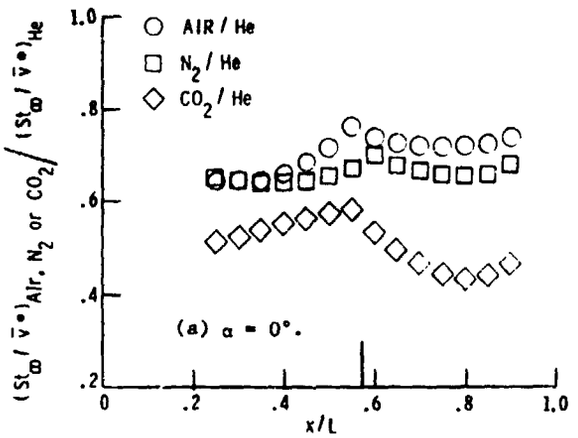

Fig. 14 Windward heating distributions in terms of a viscous-interaction parameter for on-axis biconic.

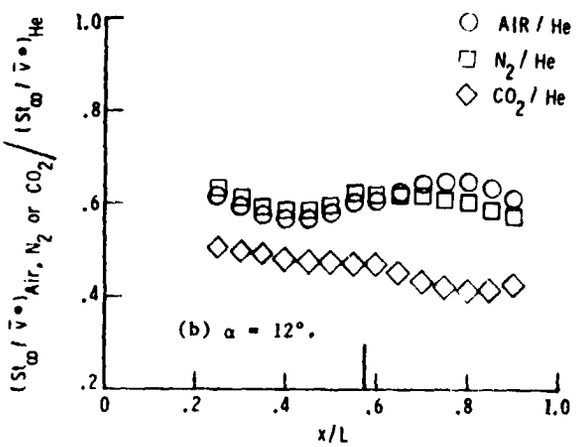

Fig. 14 Continued.

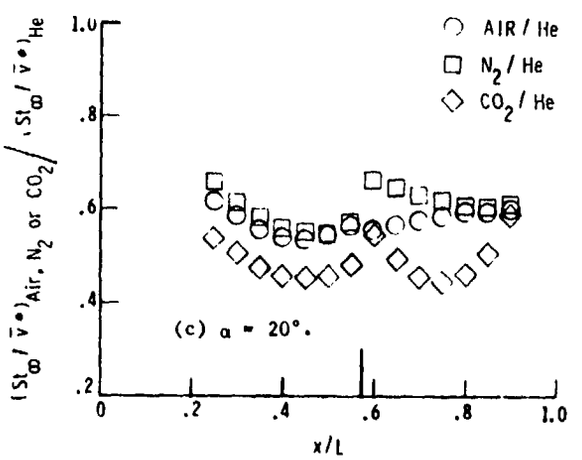

Fig. 14 Concluded.

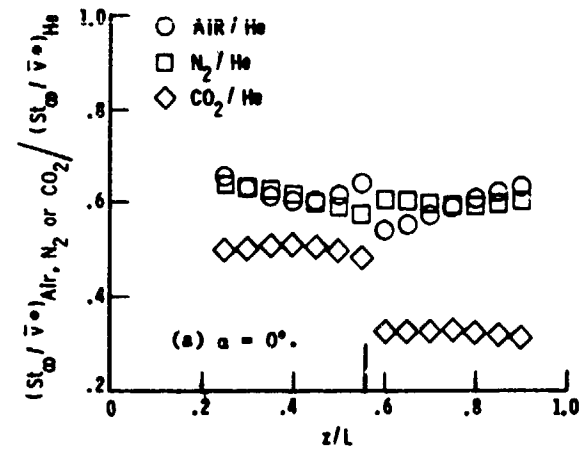

Fig. 15 Windward heating distributions in terms of a viscous-interaction parameter for bent biconic.

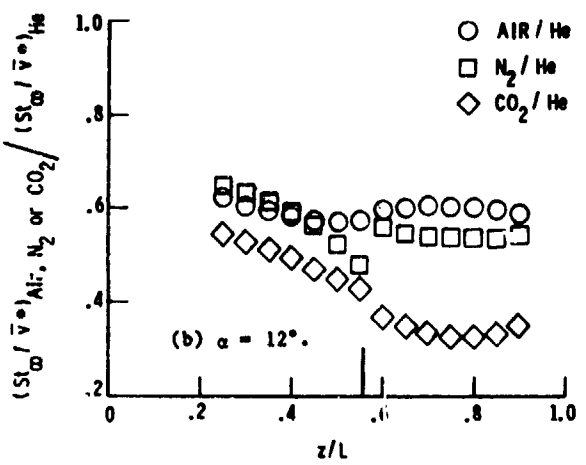

Fig. 15 Continued.

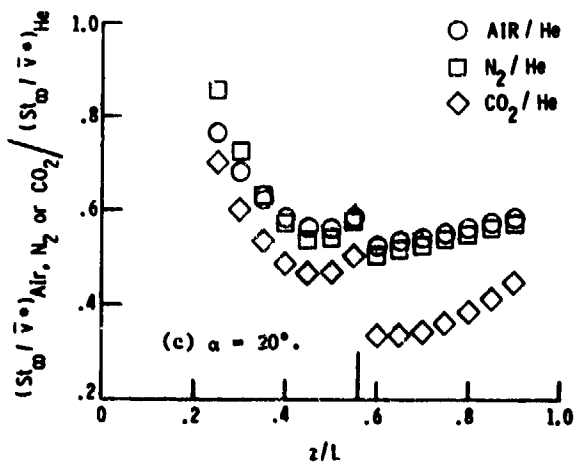

Fig. 15 Concluded.

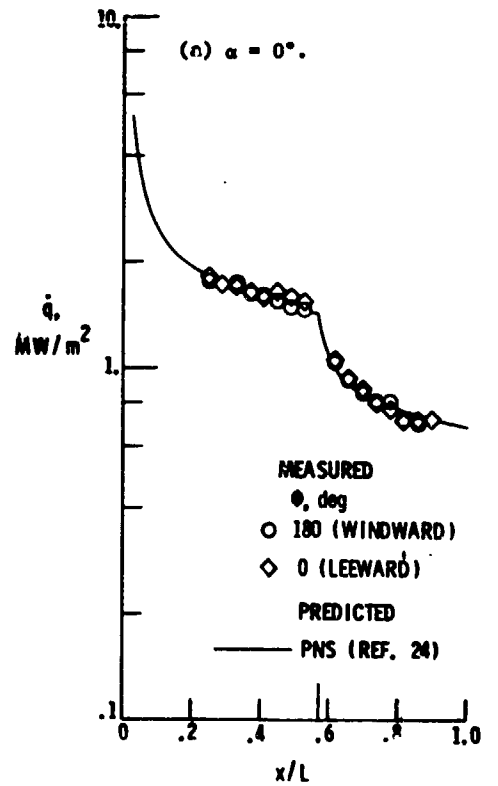

Fig. 16 Comparison of prediction to measurement for on-axis biconic in helium.

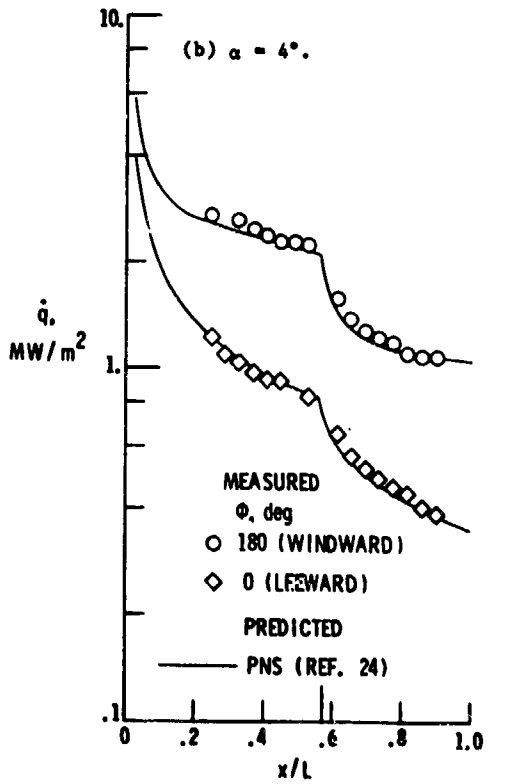

Fig. 16 Continued.

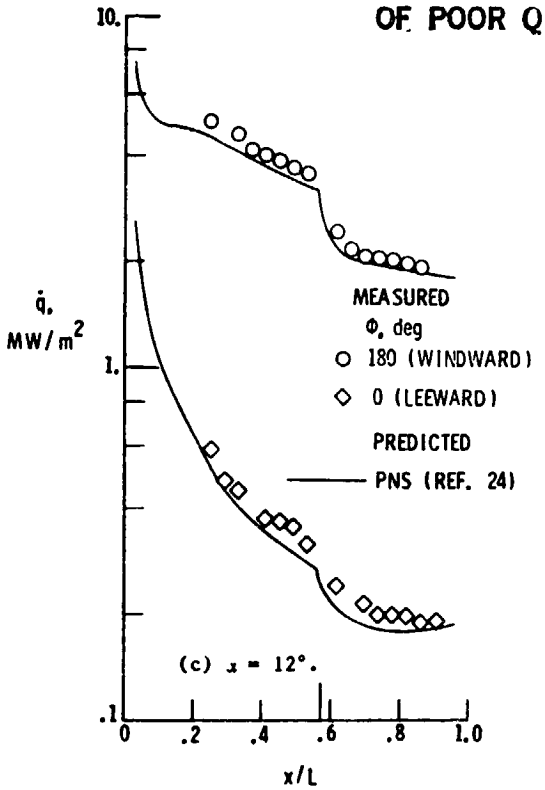

Fig. 16 Continued.

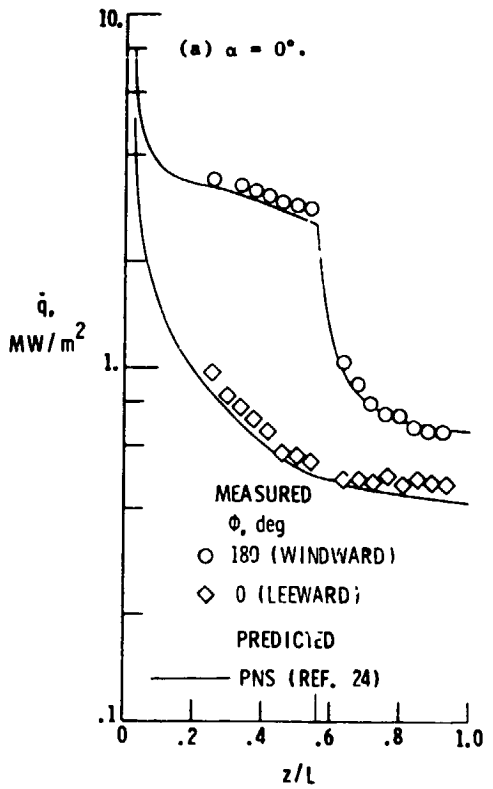

Fig. 17 Comparison of prediction to measurement for bent biconic in helium.

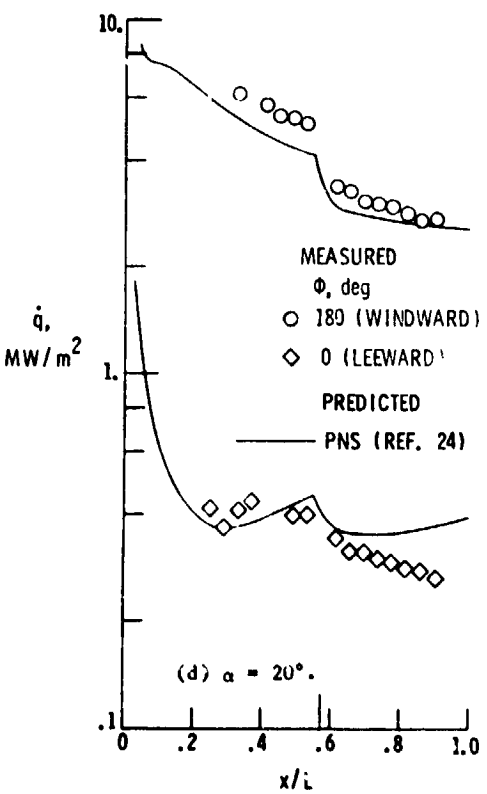

Fig. 16 Concluded.

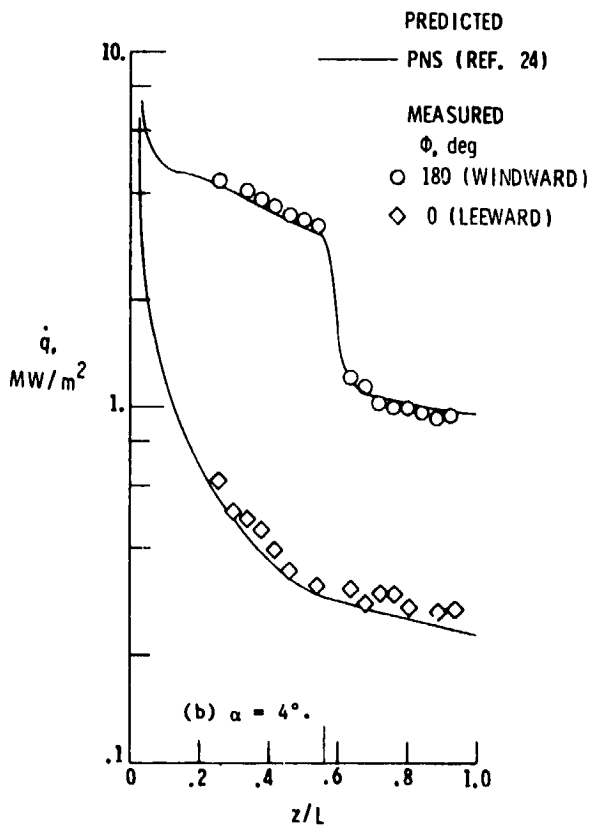

Fig. 17 Continued.

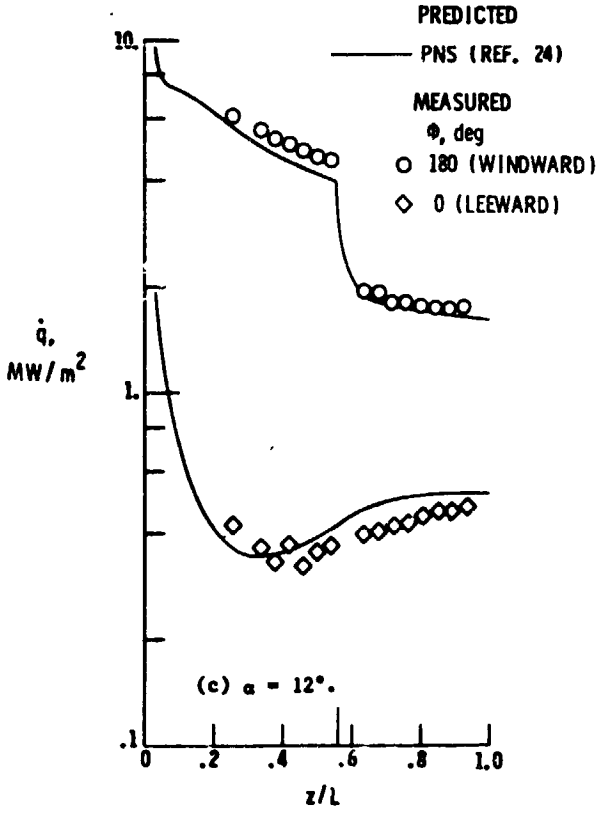

Fig. 17 Concluded.

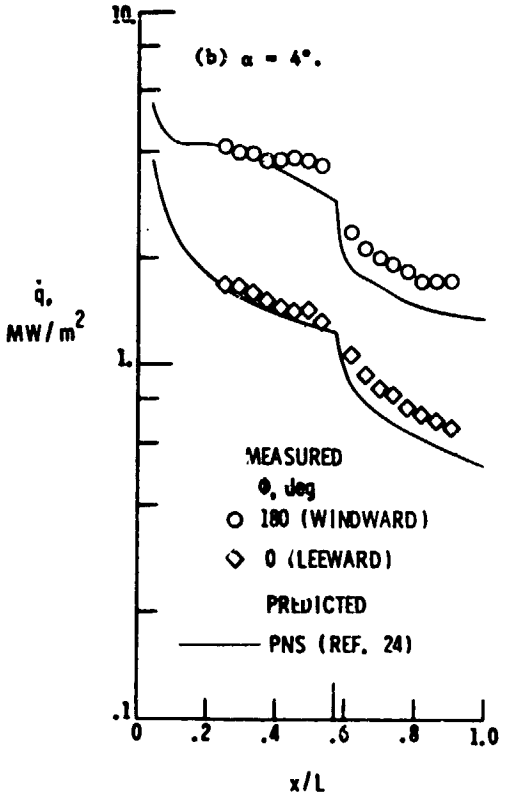

Fig. 18 Concluded.

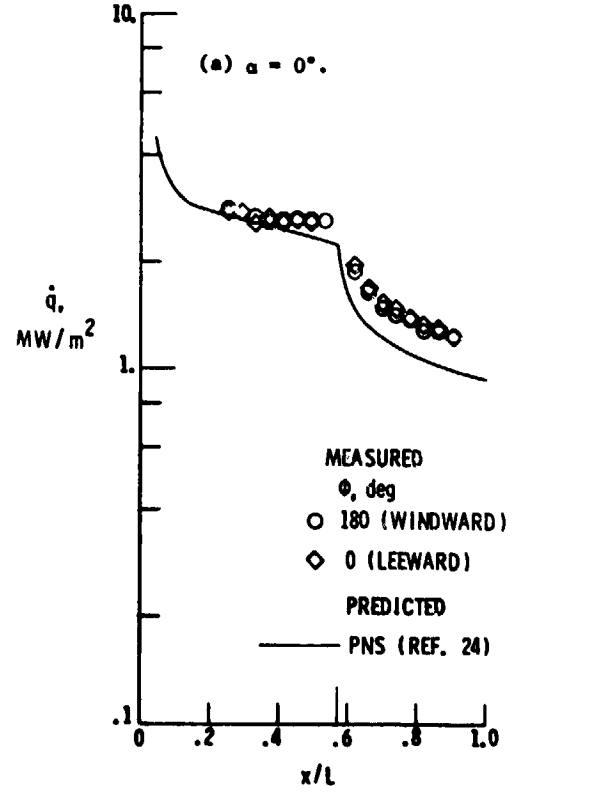

Fig. 18 Comparison of prediction to measurement for on-axis biconic in air.